Submitted to *INFORMS Journal on Computing*
manuscript (Please, provide the manuscript number!)

Authors are encouraged to submit new papers to INFORMS journals by means of a style file template, which includes the journal title. However, use of a template does not certify that the paper has been accepted for publication in the named journal. INFORMS journal templates are for the exclusive purpose of submitting to an INFORMS journal and should not be used to distribute the papers in print or online or to submit the papers to another publication.

arXiv:1907.10712v1 [math.OC] 24 Jul 2019

A nonconvex optimization approach to IMRT planning with dose-volume constraints

Kelsey Maass
Department of Applied Mathematics, University of Washington, kmaass@uw.edu

Minsun Kim
Department of Radiation Oncology, University of Washington, mk688@uw.edu

Aleksandr Aravkin
Department of Applied Mathematics, University of Washington, saravkin@uw.edu

Fluence map optimization for intensity-modulated radiation therapy planning can be formulated as a large-scale inverse problem with multi-objectives on the tumors and organs-at-risk. Unfortunately, clinically relevant dose-volume constraints are nonconvex, so convex formulations and algorithms cannot be directly applied to the problem. We propose a novel approach to handle dose-volume constraints while preserving their nonconvexity, as opposed to previous efforts which focused on iterative convexification. The proposed method is amenable to efficient algorithms based on partial minimization and naturally adapts to handle maximum and mean dose constraints, which are prevalent in current practice, and cases of infeasibility. We demonstrate our approach using the CORT dataset, and show that it is easily adaptable to radiation treatment planning with dose-volume constraints for multiple tumors and organs-at-risk.

Key words: Radiation treatment planning, nonconvex optimization
History:

1. Introduction

Radiotherapy uses high-energy ionizing radiation to eradicate cancer cells, but unfortunately, it also damages the normal tissue cells in its path. The main goal of radiation treatment planning is to maximize the differential between the damage to the tumor and healthy tissue by delivering a concentrated dose to the tumor while sparing healthy tissue nearby. The most common form of radiotherapy is external beam radiation therapy (EBRT), where photon beams generated by a linear accelerator are directed at the patient from a rotating gantry [1]. By surrounding the tumor with beams from multiple angles,

physicians can design treatment plans that target tumors with a variety of geometries while avoiding a large dose to the critical structures.

Conventional EBRT began soon after the discovery of X-rays in 1895, and was significantly impacted by technological innovations such as advanced imaging and multileaf collimators (MLC). In particular, the invention of computed tomography (CT) in the 1970s enabled accurate three-dimensional mapping of a patient's internal anatomy, while the introduction of the MLC to radiotherapy in the 1990s allowed for more precise beam shaping to match tumor outlines and reduce radiation exposure to healthy tissues. The sliding leaves of the MLC can be used to modulate beam intensities, giving more control over the patient dose distribution. Discretizing each beam into subunits, called beamlets, dramatically increased the number of variables under consideration, making the prevailing forward planning approach using trial-and-error infeasible. In 1988, the idea of "inverse planning" for intensity-modulated radiation therapy (IMRT) was introduced by Brahme [2], and mathematical optimization was used to calculate beamlet intensities that generate a specified dose. For a more detailed history of IMRT, see [3, 4, 5, 6].

1.1. Intensity-modulated radiation therapy

In current practice, the patient undergoes imaging (e.g., CT) before IMRT treatment, producing a three-dimensional model of their internal anatomy. This model is discretized into volume units (voxels) and labeled by structure. Next, the physician specifies the prescription, often in terms of a uniform target to the tumor with various constraints on critical structures. The goal of the treatment planner is then to determine the number of beams, beam angles, and beamlet intensities that will deliver the prescribed dose of radiation to the tumor while keeping doses to healthy tissues low. Inverse planning for IMRT typically involves three steps [6]:

1. Beam angles: Determine the number of beams and their orientations.
2. Fluence map: Calculate beamlet intensities to deliver the desired dose distribution to the patient.
3. Segmentation: Design MLC sequences that achieve the optimized fluence map.

These steps require solving optimization problems that can be approached separately or in combination. In this paper, we focus on the fluence map problem of assigning beamlet intensities for a given set of beams and beam angles in the presence of competing tumor and normal tissue objectives and constraints. We develop a new approach that is well

adapted to handle *nonconvex dose-volume constraints*, in addition to convex max-dose and mean-dose constraints. We first explain all three constraint types.

Radiation dose is measured in gray (Gy), where one Gy is defined as the absorption of one joule of energy per kilogram of matter. Although lower doses are always better for normal tissues, tolerable doses for many tissues are known empirically and depend on the risk level that a patient and physician are willing to accept. In practice, tolerable doses for different tissues are formulated using the following three types of constraints:

- Maximum dose: No voxel in the organ receives more than $d^{\max}$ Gy.
- Mean dose: Average radiation per voxel does not exceed d^{mean} Gy.
- Dose-volume: At most $p\%$ of the organ volume receives more than d^{dv} Gy.

Serial structures such as the spinal cord and brainstem lose functionality if any of their subvolumes are damaged, so maximum dose constraints are the best indicator of tissue damage. On the other hand, parallel structures such as the liver and lungs are composed of semi-independent units. In this case, a fraction of the parallel organ can be damaged without loss of functionality, so dose-volume constraints are appropriate [7]. Assigning maximum constraints on partial volumes to achieve the desired dose-volume criteria was first introduced by Langer and Leong in 1987 [8] and brought to the attention of the mathematical community by Shepard et al. in 1999 [3]. Maximum and mean dose constraints define a *convex* feasible region for the decision variables. The associated optimization problems can be solved at scale; in fact, inverse planning with linear inequality constraints can be formulated as a convex quadratic program, with state of the art approaches and commercial implementations readily available (see e.g., [9]).

1.2. Challenge of dose-volume constraints

In contrast to maximum and mean dose constraints, dose-volume constraints are *combinatorial*, since the choice of the $p\%$ of organ voxels that receive more than d Gy is left to the planner. In early IMRT research, using only a small number of beamlets and voxels, it was possible to solve the treatment planning problem for all possible voxel combinations satisfying a dose-volume constraint and then choose the best resulting plan [8]. This approach becomes infeasible as the problem size increases to clinically relevant situations: for an organ with n voxels and a dose-volume constraint imposed on m of these voxels, there are $n!/((n-m)!m!)$ possible voxel combinations that would satisfy the constraint [7]. The highly nonconvex nature of dose-volume constraints explains the heuristic approaches

in existing methods. Morrill et al. [10] divide organ volumes *a priori* into high and low regions based on tumor proximity. Fu et al. [11] take a two-stage approach, first solving the problem with a convex relaxation of the dose-volume constraint, and then resolving the problem with a maximum constraint imposed on the $(100-p)\%$ of the voxels in the critical structure that received the lowest dose. Llacer et al. [12] assign maximum doses dynamically: after each iteration, a maximum value of $d^{\max}$ is assigned to the $p\%$ of the voxels of the critical structure that received the highest doses, while a maximum value of d^{dv} is assigned to the remaining $(100-p)\%$ voxels. Unlike the previous two methods, they do not impose hard constraints on the voxel doses. Instead, only voxels exceeding their assigned maximum value contribute to the objective function in each iteration.

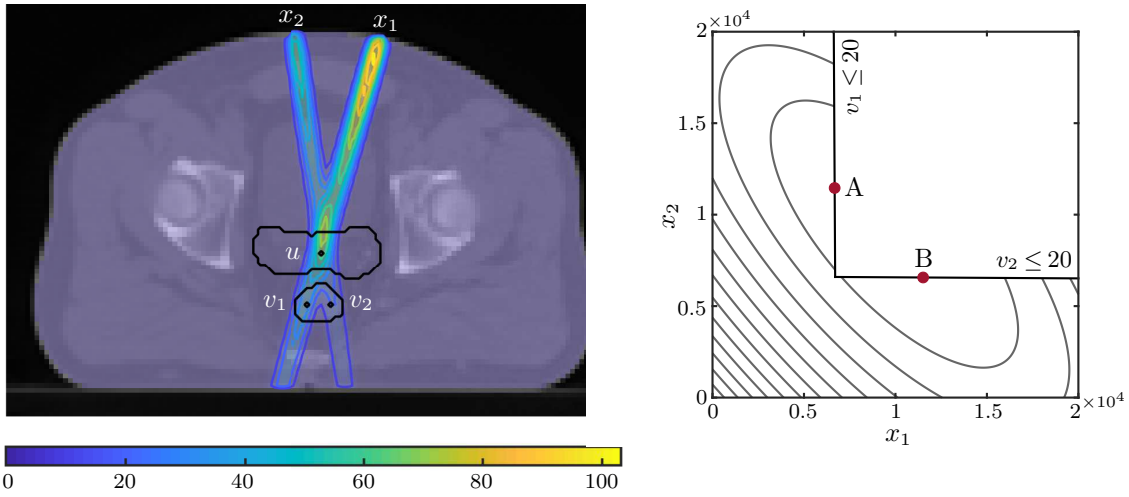


Figure 1 **Left: Three body voxels, one belonging to a prostate tumor (u) and two belonging to the rectum (v_1 and v_2), are irradiated by two beamlets (x_1 and x_2). The beamlet intensities correspond to the global minimum at point B. Right: The nonconvex feasible region induced by the dose-volume constraint that 50% of the rectum volume does not exceed 20 Gy is explicitly given by the union of regions $v_1 \leq 20$ and $v_2 \leq 20$. The contours indicate the isolines of objective function (1), with local minimum at point A and global minimum at point B.**

To illustrate the nonconvex geometry of a feasible beamlet region induced by a dose-volume constraint, we recreate an example from Wu et al. [13] using the CORT dataset described in Section 4. We consider three body voxels of the patient, where voxel u belongs to a prostate tumor and voxels v_1 and v_2 belong to the rectum (left panel of Figure 1). Using two beamlets x_1 and x_2, we would like to deliver a uniform dose of 81 Gy to the

tumor while ensuring that *no more than 50% of the rectum volume (one voxel in this case) may exceed 20 Gy.*

We calculate the optimal beamlet intensities by minimizing the objective function

$$\frac{1}{2}\|Ax - 81\|_2^2 + \frac{\lambda}{2}\|x\|_2^2 \tag{1}$$

subject to the dose-volume constraint. The matrix $A \in \mathbb{R}^{1\times 2}$ maps beamlet intensities to voxel doses, the vector $x \in \mathbb{R}^2$ contains the beamlet intensities, and the regularization term controlled by $\lambda = 5 \times 10^{-6}$ is added to stabilize beamlet solutions, amortizing the ill-conditioned beamlet-to-voxel map. In Figure 1 (right), we plot the feasible beamlet region along with the contours of the objective function. Since negative beamlet intensities are impossible, we restrict the beamlet values to the first quadrant.

There are two possibilities for satisfying the dose-volume constraint: either the first rectum voxel is allowed to exceed 20 Gy (Figure 1, $v_2 \leq 20$ line), or the second rectum voxel is allowed to exceed 20 Gy (Figure 1, $v_1 \leq 20$ line). The union of these two regions forms an L-shaped nonconvex region with two local minima at points A and B. Depending on the beamlet initialization and algorithm used to minimize the objective function, it is possible to converge to either of these two local minima, and there is no guarantee that the global minimum at B will be reached. In general, the feasible beamlet region imposed by a dose-volume constraint comprises the nonconvex union of regions satisfying maximum constraints for different choices of voxels [14].

The great watershed in optimization is between convex and nonconvex problems [15]. When minimizing a convex objective function over a convex set, all local minima are also global. Conversely, optimizing any function over a nonconvex set leads to a nonconvex problem with potentially many local minima. Even in the 2-D example in Figure 1, the dose-volume constraint creates a nonconvex feasible set where each choice of voxel corresponds to a different local minimum. To avoid converging to local minima, early IMRT treatment planning relied on stochastic algorithms such as simulated annealing, which suffered from slow convergence rates [4, 7]. Fortunately, it is often possible to find local minima whose dose distributions are close to the global minimum using fast gradient methods [12, 16], so the emphasis in IMRT is often on finding a good local minimum rather than the global minimum [12, 13, 16, 17, 18].

1.3. Contributions

In this paper, we develop a novel approach to handle dose-volume constraints in the radiation treatment planning problem. In contrast to prior efforts, which focused on iterative convexification, our formulation is nonconvex, yet can be efficiently solved using continuous optimization techniques. We start with the idealized problem, formulated using objectives for the tumor and constraints for the organs-at-risk (OARs), and extend it to a flexible formulation that allows re-weighting strategies to balance infeasible solutions (with respect to the OARs) against delivering a sufficient amount of radiation to the tumor. To solve this formulation, we develop a customized algorithm that combines quadratic programming with fast nonlinear operators, and guaranteed to converge to a stationary point of the proposed model. The overall approach is scalable, handles multiple objectives on tumors and OARs, and returns actionable treatment plans on patient-scale datasets.

The paper proceeds as follows. In Section 2 we formulate radiation treatment planning as a nonconvex optimization problem over the fluence map. In Section 3 we develop a custom optimization algorithm and provide a convergence analysis. In Section 4 we present multiple radiation treatment use cases with data from an anonymized cancer patient dataset. Finally, in Section 5 we summarize the results and discuss future avenues for research.

2. Problem Formulation

Given a fixed number of beams and beam angles, the dose delivered to the patient is approximated with a linear mapping from beamlet intensity to voxel dose. The inverse planning step is to calculate beamlet intensities that achieve the desired dose distribution to planning target volumes (PTVs) indexed by $i \in I$, while respecting constraints on OARs indexed by $j \in J$. Let d_i denote target delivery doses (often in Gy) to PTV $i \in I$, and $d_j^{\max}$, d_j^{mean}, and d_j^{dv} denote the max, mean, and dose-volume tolerance values for OAR $j \in J$. The set of OARs that have max, mean, and dose-volume constraints is denoted by $J^{\max}, J^{\text{mean}}$, and J^{dv}. Let A_i and A_j be the linear beamlet-to-voxel maps for the PTV i and OAR j. The variable x encodes the unknown vector of beamlet intensities (which must be nonnegative). The idealized fluence map inverse problem with a uniform dose on the PTVs and the three constraints described in Section 1 on the OARs is given by

$$(\mathcal{P}_0) \quad \underset{x \geq 0}{\text{minimize}} \quad \sum_{i \in I} \frac{\alpha_i}{2n_i} \|A_i x - d_i\|_2^2 + \frac{\lambda}{2} \|x\|_2^2 \tag{2a}$$

$$\text{subject to} \quad A_j x \le d_j^{\max}, \qquad j \in J^{\max}, \tag{2b}$$

$$\mathbf{1}^T A_j x \le n_j d_j^{\text{mean}}, \qquad j \in J^{\text{mean}}, \tag{2c}$$

$$\|(A_j x - d_j^{\text{dv}})_+\|_0 \le \frac{n_j p_j}{100}, \quad j \in J^{\text{dv}}. \tag{2d}$$

where n_i and n_j indicate total voxels in the ith PTV and jth OAR, and $\lfloor(\frac{n_j p_j}{100})\rfloor$ is the number of voxels in the jth OAR that may receive a dose exceeding d_j^{dv}. The dose-volume constraint (2d) forces the number of voxels receiving a dose greater than d_j^{dv} to be less than p_j percent of the total voxels:

$$\|(A_j x - d_j^{\text{dv}})_+\|_0 = \|\max\{0, A_j x - d_j^{\text{dv}}\}\|_0 = \text{number of voxels s.t. } A_j x > d_j^{\text{dv}}.$$

The least-squares term used for the uniform target dose is widely used [6]. In principle, Problem $(\mathcal{P}_0)$ can be replaced by a feasibility problem, with lower and upper dose-volume constraints also placed on the PTV. Here we focus on $(\mathcal{P}_0)$ but the techniques we propose extend to the feasibility problem.

Problem $(\mathcal{P}_0)$ is difficult for several reasons. First, it is high-dimensional (beamlets can be on the order of $10^3 - 10^5$) [13]. Second, beamlet-to-voxel maps are ill-conditioned [4]. Third, dose-volume constraints are combinatorial in nature, and finding the global solution is NP-hard. Solving Problem $(\mathcal{P}_0)$ requires making a choice of voxels allowed to exceed d_j^{dv}. Finally, while the Problem $(\mathcal{P}_0)$ is always feasible (i.e. $x = 0$ is a solution), it may not yield a clinically useful radiation distribution. Feasibility-type reformulations of $(\mathcal{P}_0)$ often fail to have any meaningful solutions because the target doses almost always compete with OAR doses, as it is common for tumors to be close to or within OARs. Practical radiation treatment planning converts constraints into objectives, and then looks for the best trade-off among competing objectives.

In the next section, we formulate the idealized problem using constraints, and then develop a relaxation that always has a feasible solution. This allows significant modeling and computational flexibility, yielding efficiently computable and clinically useful solutions that balance the need to deliver enough radiation to the tumor while approximately satisfying OAR constraints.

2.1. New formulation

To simplify the exposition, we explain the new formulation using only dose-volume constraints on the OARs:

$$\begin{array}{ll} \underset{x \geq 0}{\text{minimize}} & \displaystyle\sum_{i \in I} \frac{\alpha_i}{2n_i} \|A_i x - d_i\|_2^2 + \frac{\lambda}{2}\|x\|_2^2 \\ \text{subject to} & \|(A_j x - d_j^{\text{dv}})_+\|_0 \leq \dfrac{n_j p_j}{100}, \quad j \in J^{\text{dv}}. \end{array} \tag{3}$$

Solutions to (3) may not be clinically useful if the dose-volume constraints prevent sufficient dose delivered to the tumor. We develop an extended, nonconvex formulation that relaxes the dose-volume constraints. The new formulation includes additional variables $w_j \approx A_j x - d_j^{\text{dv}}$, and penalizes deviations of the delivered OAR doses from w_j:

$$\begin{array}{ll} \underset{x \geq 0,\, w}{\text{minimize}} & f(x,w) := \displaystyle\sum_{i \in I} \frac{\alpha_i}{2n_i} \|A_i x - d_i\|_2^2 + \sum_{j \in J^{\text{dv}}} \frac{\alpha_j}{2n_j} \|w_j - (A_j x - d_j^{\text{dv}})\|_2^2 + \frac{\lambda}{2}\|x\|_2^2 \\ \text{subject to} & \|(w_j)_+\|_0 \leq \dfrac{n_j p_j}{100}, \quad j \in J^{\text{dv}}. \end{array} \tag{4}$$

In formulation (4), the auxiliary variables w_j are forced to satisfy the dose-volume constraints, while the residuals $A_j x - d_j^{\text{dv}}$ may not necessarily do so. The weights α_j control how closely w_j must approximate $A_j x - d_j^{\text{dv}}$, and as $\alpha_j \uparrow \infty$, problem (4) converges to the idealized problem (3).

Formulation (4) has several desirable features. First, it has all the flexibility of the heuristic approaches described in the introduction. Just as in [12], the particular voxels allowed to exceed d_j^{dv} are allowed to change within each iteration. However, this happens automatically as the optimization proceeds. Second, (4) fully captures the nonconvex structure of dose-volume constraints, while giving the modeler flexibility to match them approximately using weights α_j. The weights α_i and α_j can be tuned to balance the tradeoff between covering the tumor and approximately meeting OAR constraints. Finally, from a computational perspective, we can design efficient and provably convergent algorithms that aggregate information from multiple tumors and OARs using partial minimization, as described in the next section.

3. Algorithmic Approach

Our main strategy is to *partially minimize* formulation (4) with respect to x, viewing (4) as a *value-function optimization* problem

$$\begin{aligned} \underset{w}{\text{minimize}} \quad & g(w) := \min_{x \geq 0} \sum_{i \in I} \frac{\alpha_i}{2n_i} \|A_i x - d_i\|_2^2 + \sum_{j \in J^{\text{dv}}} \frac{\alpha_j}{2n_j} \|w_j - (A_j x - d_j^{\text{dv}})\|_2^2 + \frac{\lambda}{2} \|x\|_2^2 \\ \text{subject to} \quad & w_j \in \Omega_j := \left\{ \|(w_j)_+\|_0 \leq \frac{n_j p_j}{100} \right\}, \quad j \in J^{\text{dv}}. \end{aligned} \tag{5}$$

The algorithm is centered on optimizing the value function $g(w)$ in (5), using a projected gradient approach to take care of the nonconvex constraints encoded by Ω_j. The high-level iteration is simply

$$w^{(k)} = \text{proj}_{\Omega}(w^{(k-1)} - \beta \nabla g(w^{(k-1)})), \tag{6}$$

where $w = [w_1, \ldots, w_J]$ and $\Omega = \Omega_1 \otimes \cdots \otimes \Omega_J$. Evaluation of g and ∇g is done through computing the partial minimum over x, as detailed in Algorithm 1. Projection onto Ω_j is implemented by keeping all negative entries and the largest $\lfloor (\frac{n_j p_j}{100}) \rfloor$ positive entries of w_j unchanged, and sending the remaining positive entries to 0.

The differentiability of $g(w)$, formula for the derivative, and its Lipschitz constant follow from [19, Theorem 1]. In particular, for one PTV and one OAR, define

$$g(w) = \min_{x \geq 0} \frac{\alpha_1}{2n_1} \|A_1 x - d_1\|_2^2 + \frac{\alpha_2}{2n_2} \|w - (A_2 x - d_2^{\text{dv}})\|_2^2 + \frac{\lambda}{2} \|x\|_2^2.$$

Next, taking $h(x) = \delta_{x \geq 0}(x) + \frac{1}{2}\|A_1 x - d_1\|_2^2 + \frac{\lambda}{2}\|x\|_2^2$, where $\delta_{x \geq 0}(x)$ is the indicator function of the nonnegative orthant, from [19, Theorem 1] we have

$$\begin{aligned} \nabla g(w) &= \frac{\alpha_2}{n_2}(w - A_2(x(w) - d_2^{\text{dv}})), \\ x(w) &\in \arg\min \frac{\alpha_2}{2n_2} \|w - (A_2 x - d_2^{\text{dv}})\|_2^2 + h(x), \\ \text{lip}(\nabla g(w)) &\leq \frac{\alpha_2}{n_2}. \end{aligned}$$

Algorithm 1 is projected gradient descent for the value function (5), and is equivalent to the simple iteration (6). The prox-gradient method with a nonconvex regularizer converges (with respect to a stationarity measure) with a rate proportional to $\frac{\text{lip}(\nabla g)}{\sqrt{k}}$ (apply e.g., [20, Theorem 1]). If we choose particular stepsizes $t_j = \frac{n_j}{\alpha_j}$, Algorithm 1 reduces to block-coordinate descent, detailed in Algorithm 2, and so its convergence follows immediately by equivalence to the prox-gradient method for the value function $g(w)$.

Algorithm 1 Proximal gradient for $g(w)$ in (5).

Input $x^{(0)}, \epsilon$. Initialize $k=0$, $w_j^{(0)} = \text{proj}_{\Omega_j}\left(A_j x^{(0)} - d_j^{\text{dv}}\right)$. Set $t_j \leq \frac{n_j}{\alpha_j}$.

while err $> \epsilon$ **do**

$k = k+1$

$x^{(k)} = \arg\min_{x \geq 0} f\left(x, w^{(k-1)}\right)$

for $j \in J^{\text{dv}}$ **do**

$w_j^{(k)} = \text{proj}_{\Omega_j}\left(w_j^{(k-1)} - \frac{\alpha_j t_j}{n_j}\left(w_j^{(k-1)} - \left(A_j x^{(k)} - d_j^{\text{dv}}\right)\right)\right)$

end for

$\text{err} = \sum_{j \in J^{\text{dv}}} \frac{1}{t_j} \left\| w_j^{(k)} - w_j^{(k-1)} \right\|_2$

end while

return $\arg\min_{x \geq 0} f\left(x, w^{(k)}\right)$

Algorithm 2 Block coordinate descent: special case of Algorithm 1 with $t_j = \frac{n_j}{\alpha_j}$.

Input $x^{(0)}, \epsilon$. Initialize $k=0$, $w_j^{(0)} = \text{proj}_{\Omega_j}\left(A_j x^{(0)} - d_j^{\text{dv}}\right)$. Set $t_j = \frac{n_j}{\alpha_j}$.

while err $> \epsilon$ **do**

$k = k+1$

$x^{(k)} = \arg\min_{x \geq 0} f\left(x, w^{(k-1)}\right)$

for $j \in J^{\text{dv}}$ **do**

$w_j^{(k)} = \text{proj}_{\Omega_j}\left(A_j x^{(k)} - d_j^{\text{dv}}\right)$

end for

$\text{err} = \sum_{j \in J^{\text{dv}}} \frac{1}{t_j} \left\| w_j^{(k)} - w_j^{(k-1)} \right\|_2$

end while

return $\arg\min_{x \geq 0} f\left(x, w^{(k)}\right)$

3.1. Simple example

To demonstrate how the relaxed formulation (4) and Algorithm 2 behaves compared to the idealized problem (3), we revisit our example from the introduction. For iterations $k = 0, 3, 32$ of Algorithm 2 to solve (4), we plot the contour lines of the objective function

$$f(x, w^{(k)}) = \frac{1}{2}\|A_1 x - 81\|_2^2 + \frac{5}{2}\|w^{(k)} - (A_2 x - 20)\|_2^2 + \frac{\lambda}{2}\|x\|_2^2 \tag{7}$$

in terms of the beamlet intensity variable x for fixed $w^{(k)}$. Here $A_1 \in \mathbb{R}^{1\times 2}$ and $A_2 \in \mathbb{R}^{2\times 2}$ are the beamlet-to-voxel maps for the prostate tumor and rectum, $x \in \mathbb{R}^2$ contains the beamlet

intensities, $w^{(k)} \in \mathbb{R}^2$ approximates the deviation between the dose received by the rectum and the dose-volume constraint, and λ is set at 5×10^{-6}. In each figure, $x^{(k+1)}$ corresponds to the global minimum of the relaxed problem at iteration k, A and B correspond to the local and global minima of the idealized problem, and the nonconvex feasible region induced by the dose-volume constraint that 50% of the rectum volume does not exceed 20 Gy is given by the union of regions $v_1 \leq 20$ and $v_2 \leq 20$.

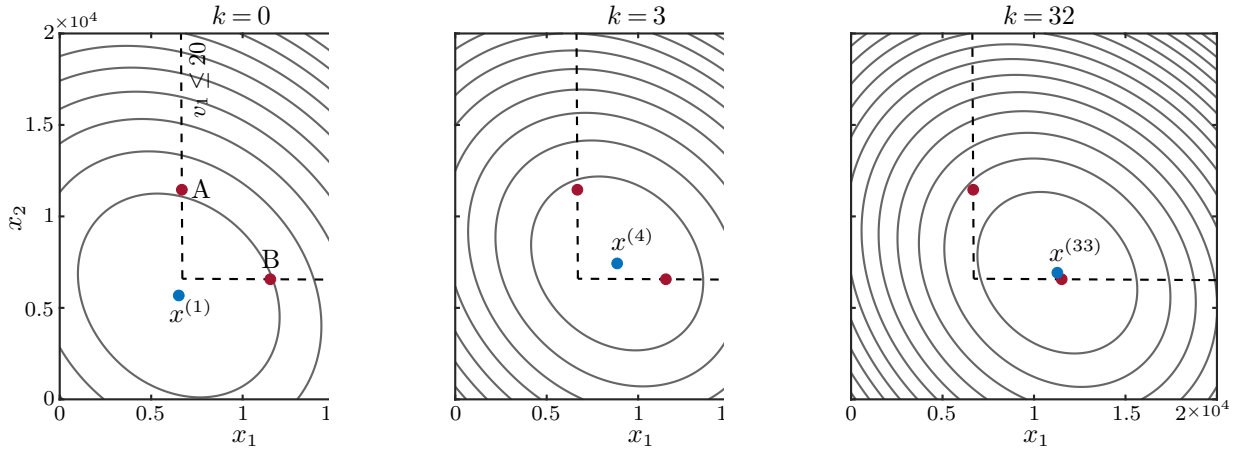


Figure 2 **Contours of (7) in x for fixed iterates $w^{(k)}$ with $k = 0, 3, 32$. The points A and B correspond to the local and global minima of the idealized problem (3). Starting with the zero vector $x^{(0)}$, the global minimum of the relaxed problem ($x^{(k+1)}$) moves towards the global minimum of the idealized problem (B).**

In Figure 2 (left), we initialize the problem with $x^{(0)}$ as the zero vector. The contours of (4) are more circular than those of (3) in Figure 1, indicating that the relaxation has improved the problem conditioning. Additionally, as $w^{(k)}$ changes with each iteration, the global minimum of the objective function in terms of x at point $x^{(k+1)}$ moves closer to the global minimum of (3) at point B. For stopping tolerance $\epsilon = 10^{-3}$, our algorithm converges after 32 iterations, and in Figure 2 (right) we see that the global minimum of our relaxed problem, corresponding to our final beamlet intensities, is just shy of the global minimum of our original problem. The dose-volume constraint is met approximately, and we may choose larger weight coefficient α_2 or decrease the dose level d_2^{dv} to move closer to the feasible region if necessary.

Next, we plot our iterates along with the contour lines of the objective function

$$g(w) = \min_{x \geq 0} \frac{1}{2}\|A_1 x - 81\|_2^2 + \frac{5}{2}\|w - (A_2 x - 20)\|_2^2 + \frac{\lambda}{2}\|x\|_2^2 \tag{8}$$

in terms of the variable w. In Figure 3, points A and B again correspond to the local and global minima of the idealized problem, and the nonconvex feasible region $\Omega = \{\|w_+\|_0 \leq$

0.5} is given by the union of regions $w_1 \leq 0$ and $w_2 \leq 0$. The first three iterates lie within Ω, so the result of the gradient step before and after projection onto Ω are equal. However, for iterates 4 - 32, we see the result of the gradient step as orange squares, and the projection onto Ω as blue circles. Just as we saw in x-space, our algorithm in w-space converges to a point near the global minimum at B.

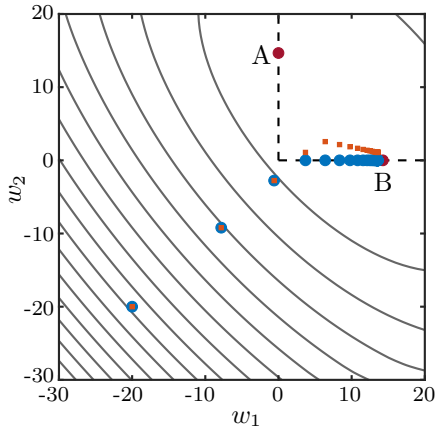


Figure 3 **Contours of (8) with respect to w. The points A and B correspond to the local and global minima of the idealized problem (3), the squares correspond to the iterates $w^{(k)}$ before projection onto the feasible set Ω, and the circles correspond to the iterates after projection. Starting with the zero vector $x^{(0)}$, we converge after 32 iterations at a point near the global minimum at B.**

3.2. Initialization

Because our formulation is nonconvex, the initialization can affect both the solution and the time to convergence. For example, using the initialization $x^{(0)} = (0, 2 \times 10^3)^T$ for our simple example, we converge near the local minimum at A after 37 iterations (left panel of Figure 4). Fortunately, as demonstrated in other papers (see e.g., [12, 16]), local minima do not have a large effect on the solutions to these least-squares formulations, especially when the convex tumor term dominates the model [18]. Given enough time, different initializations tend to converge to similar objective values, fluence maps, and dose distributions.

For the remainder of our examples, we initialize the beamlet intensity vector as the solution to (4) without any dose-volume terms, i.e.,

$$x^{(0)} = \arg\min_{x \geq 0} \sum_{i \in I} \frac{\alpha_i}{2n_i} \|A_i x - d_i\|_2^2 + \frac{\lambda}{2} \|x\|_2^2. \tag{9}$$

In Figure 4 (right), we use this initialization for our simple example, converging near the global minimum at B after 26 iterations. For this initialization, we see that $A_2 x^{(0)} - 20$,

the value of $w^{(0)}$ before projection onto Ω, corresponds to the global minimum of $g(w)$. This is true for the general problem (4) as well. Specifically, for all $j \in J^{\mathrm{dv}}$ we have

$$\arg\min_{w_j} f(x,w) = A_j x - d_j^{\mathrm{dv}},$$

which means that

$$\min_{w} f(x,w) = \sum_{i\in I} \frac{\alpha_i}{2n_i}\|A_i x - d_i\|_2^2 + \frac{\lambda}{2}\|x\|_2^2.$$

Therefore letting $x^{(0)} = \min_{x\geq 0}(\min_w f(x,w))$, we are guaranteed that

$$A_j x^{(0)} - d_j^{\mathrm{dv}} = \arg\min_{w_j} g(w)$$

for all $j \in J^{\mathrm{dv}}$ because

$$\min_{x\geq 0}\left(\min_{w} f(x,w)\right) = \min_{w} g(w).$$

Since we are ultimately interested in solving $\min_{w\in\Omega} g(w)$, using an initialization for $x^{(0)}$ that corresponds to $w^{(0)} = \mathrm{proj}_\Omega(\arg\min_w g(w))$ is a natural choice.

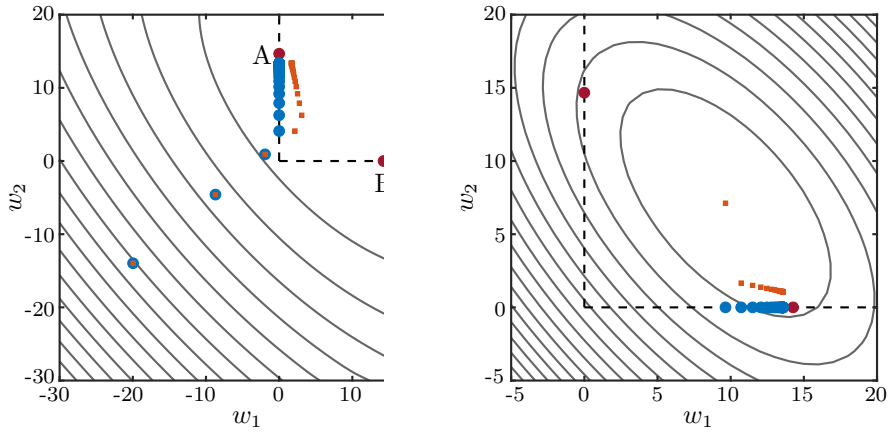


Figure 4 **Contours of (8) with respect to w. The points A and B correspond to the local and global minima of the idealized problem (3), the squares correspond to the iterates $w^{(k)}$ before projection onto the feasible set Ω, and the circles correspond to the iterates after projection. Left: Starting with the initialization $x^{(0)} = (0, 2\times 10^3)^T$, we converge near the local minimum at A after 37 iterations. Right: Starting with the initialization $x^{(0)} = \arg\min_{x\geq 0} \frac{1}{2}\|A_1 x - 81\|_2^2 + \frac{\lambda}{2}\|x\|_2^2$, we converge near the global minimum at B after 26 iterations.**

4. Numerical Results

Our examples are performed on data from an anonymized prostate cancer patient included in the CORT Dataset [21]. The dataset includes beamlet-to-voxel maps for beam angles ranging from 0° to 358° in increments of 2°, PTVs in the prostate and lymph nodes, and OARs including the rectum, bladder, femoral heads, and unspecified tissue (Figure 5). For a fixed set of beams, we consider the problem of treating tumors with dose-volume constraints of increasing difficulty on various combinations of critical structures. In Section 4.1, we look at an example with one PTV and one OAR, and show how the proposed approach works for a single dose-volume constraint on the OAR. In Section 4.2 we increase the complexity of the previous example by imposing multiple dose-volume constraints on the same OAR. Finally, in Section 4.3 we show how the approach handles multiple PTVs and OARs. For all of our examples, we use seven equally spaced beams with angles ranging from 0° to 312° in increments of 52°. We set our regularization parameter at $\lambda = 10^{-8}$, our stopping tolerance at $\epsilon = 5 \times 10^{-5}$, and for simplicity we let $\alpha_i = \alpha_j = 1$ for all $i \in I$ and all $j \in J^{\mathrm{dv}}$. Whenever there is overlap between PTVs and OARs, the voxels in common are assigned to the PTV. However, this choice is not required for our model, and a single voxel may be assigned to multiple structures if desired.

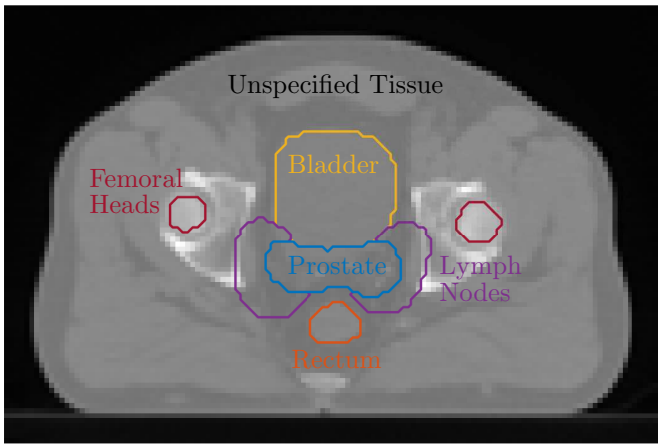


Figure 5 **Organs from the CORT prostate case on a representative axial CT slice. The prostate corresponds to planning target volume 68 (PTV_68) in the CORT dataset, while the lymph nodes correspond to planning target volume 56 (PTV_56).**

We use the cumulative dose-volume histogram as a way of evaluating the quality of the resulting treatment plans. In a dose-volume histogram, each point represents the percent of

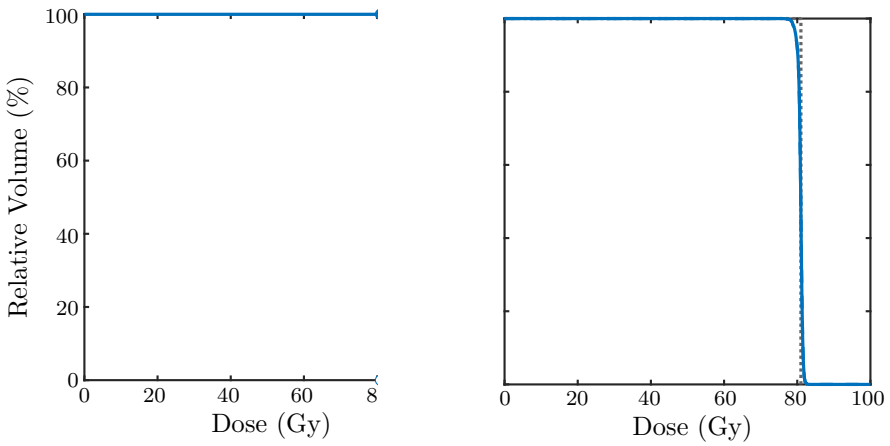


Figure 6 **Cumulative dose-volume histograms for a uniform PTV prescription of 81 Gy. Left: An ideal dose profile, with 100% of the target volume receiving exactly 81 Gy. Right: A more realistic dose profile, corresponding to our initialization for Sections 4.1 and 4.2, obtained by solving** (9) **for one prostate tumor with regularization parameter** $\lambda = 10^{-8}$.

the organ volume that receives at least a particular dose. For example, we aim to deliver a uniform dose of 81 Gy to the prostate tumor, corresponding to the dose-volume histogram on the left panel of Figure 6. In this case, exactly 100% of the organ volume receives 81 Gy. As we cannot deliver a perfectly uniform dose, our goals is to find a treatment plan that is as close as possible to this idealized dose profile. For instance, in the right panel of Figure 6 we see the dose-volume histogram of the solution to (9) for one prostate tumor with regularization parameter $\lambda = 10^{-8}$. We use the beamlet intensities from this solution as our initialization for our examples in Sections 4.1 and 4.2.

Cumulative dose-volume histograms can be used to determine whether or not an upper dose-volume constraint on an OAR has been met by a particular treatment plan. For example, we consider the dose-volume constraint that 50% of the rectum volume does not exceed 50 Gy. In Figure 7, the rectangular region within the dotted lines contains all points where at most 50% of the rectum volume receives more than 50 Gy. Therefore any dose curve that lies outside of the box does not meet the constraint, while any curve that travels inside the box meets the constraint. In the left panel of Figure 7, about 58% of the rectum volume receives more than 50 Gy, so the dose-volume constraint is not met. However, on the right panel of Figure 7 only about 42% of the rectum volume receives more than 50 Gy, so the dose-volume constraint is met.

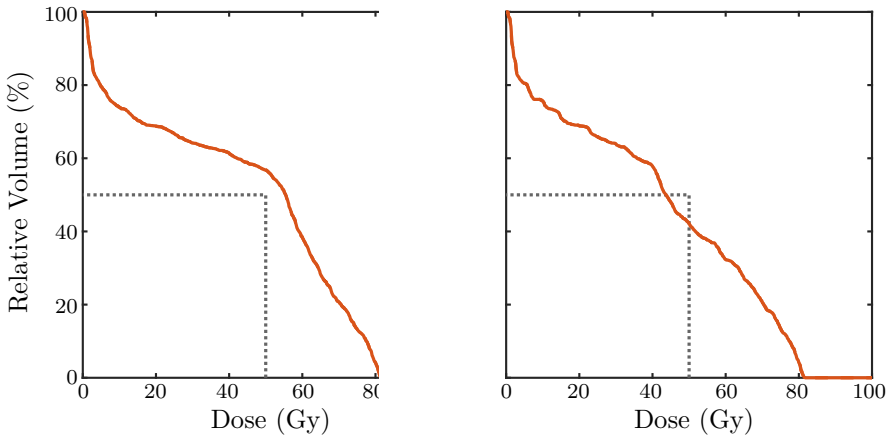


Figure 7 **Cumulative dose-histograms for an OAR dose-volume constraint that 50% of the rectum volume does not exceed 50 Gy. The solid lines correspond to the dose that the organ received, and the dotted lines enclose the region that satisfies the dose-volume constraint. Left: A treatment plan that does not meet the dose-volume constraint, with approximately 58% of the organ volume exceeding 50 Gy. Right: A treatment plan that does meet the dose-volume constraint, with approximately 42% of the organ volume exceeding 50 Gy.**

4.1. One PTV and one OAR with one dose-volume constraint

For our first example, we consider the problem of delivering a uniform dose of 81 Gy to a prostate tumor, while satisfying the dose-volume constraint that no more than 50% of the rectum volume receives more than 50 Gy. In this case, we use the linear beamlet-to-voxel maps $A_1 \in \mathbb{R}^{6670\times 986}$ and $A_2 \in \mathbb{R}^{1764\times 986}$ for the PTV and OAR respectively, with corresponding dose vectors $d_1 = 81\cdot\mathbf{1} \in \mathbb{R}^{6770}$ and $d_2^{\text{dv}} = 50\cdot\mathbf{1} \in \mathbb{R}^{1764}$. Our decision variables are $x \in \mathbb{R}^{986}$, corresponding to the 986 nonnegative beamlet intensities, and $w \in \mathbb{R}^{1764}$, corresponding to the deviation between the dose received by the rectum and the dose-volume constraint.

Figure 8 shows the behavior of our model using Algorithm 2. The objective $f(w)$ decreases monotonically (top left), and Algorithm 2 converges after 231 iterations. The tradeoff between the competing PTV and OAR objectives is shown in middle and bottom left panels of Figure 8. Because our initial beamlet intensities correspond to a solution with no dose-volume constraints, at initialization the tumor term achieves its lowest value and the rectum term achieves its highest value. Once we begin iterating, the inclusion of the OAR term causes the tumor term value to increase and the rectum term to decrease.

On the right panel of Figure 8, we show the behavior of the auxiliary variable w and our approximation of the dose-volume constraint. The difference between iterates decreases in a manner similar to the objective value (top right). the percent of rectum voxels exceeding

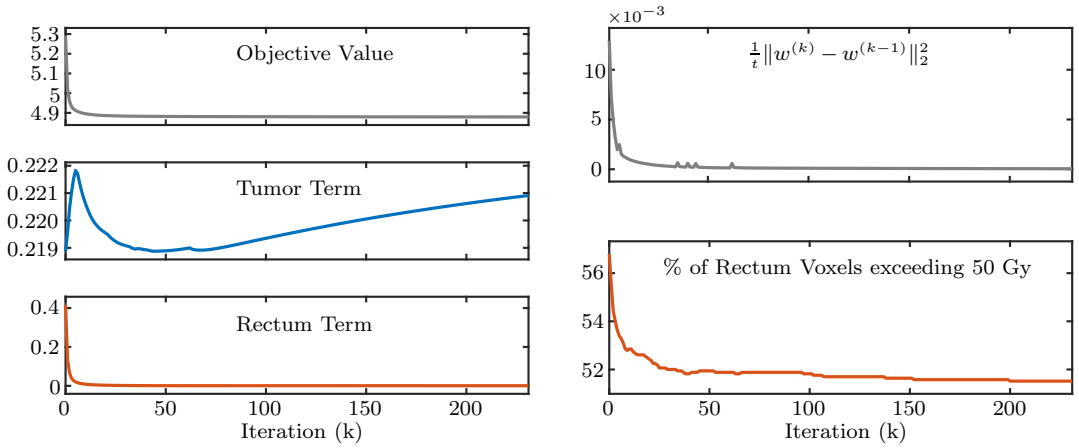


Figure 8 **Convergence of Example 4.1 using Algorithm 2. Right: Iterates the objective function $g(w)$ and individual organ terms (tumor term = $\frac{1}{2\times 6770}\|A_1x - 81\|_2^2$ and rectum term = $\frac{1}{2\times 1764}\|w - (A_2x - 50)\|_2^2$). While both $g(w)$ (top) and the rectum term (bottom) steadily decrease, the tumor term (middle) adjusts to accommodate the competing OAR objective. Right: Convergence of the auxiliary variable w (top) and our approximation of the dose-volume constraint (bottom).**

50 Gy approaches the dose-volume constraint (bottom right). Because of the relaxation, we do not meet the dose-volume constraint exactly, but we improve upon the initialization value according to the tradeoff implicitly specified by our weights α_1, α_2 and regularization parameter λ.

We can also see this approximation of the dose-volume constraint in the cumulative dose-volume histograms for the PTV and OAR in Figure 9. Here the uniform target and dose-volume constraint are shown with dotted lines, the initial dose with dashed lines, and the final dose with solid lines. There is no notable difference between the initial tumor dose and the final tumor dose (left), and we have reduced the dose to the rectum to approximately satisfy the dose-volume constraint (right). The constraint has been roughly met, with only 51.52% percent of the volume receiving more than 50 Gy, in contrast to the initialization, where 56.8% percent of the volume exceeds 50 Gy.

In Figure 10, we see a slice of the calculated dose along with the intensities of four of the beams (due to symmetry, the remaining three beams have similar intensity patterns). In this slice, it appears that a nearly uniform dose of 81 Gy is delivered to the tumor, while much of the rectum volume receives more than 50 Gy. In fact, in our solution the regions of the rectum that receive less than 50 Gy are on slices closer to the head and feet, while the region that receives more than 50 Gy lies in the middle.

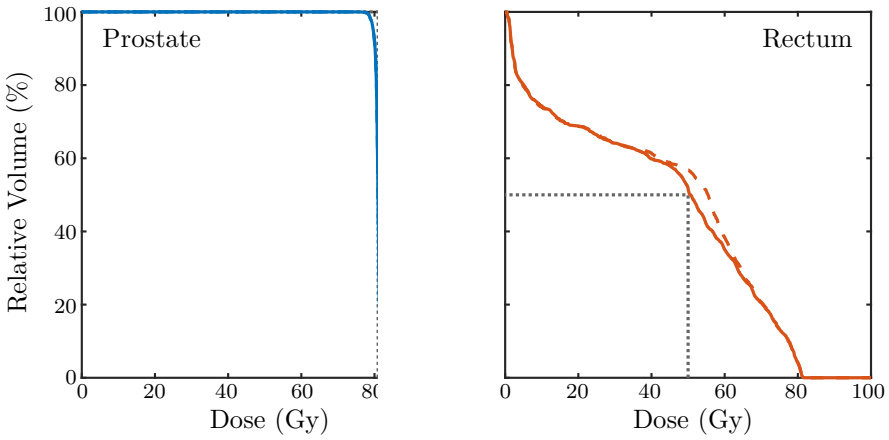


Figure 9 **Cumulative dose-volume histograms for Example 4.1. Uniform target and dose-volume constraint are denoted by dotted lines, the initial dose by dashed lines, and the final dose by solid lines. Left: There is no notable difference between the initial and final dose to the PTV. Right: The constraint that no more than 50% of the OAR volume receives mo the volume exceeds 50 Gy, as opposed to the ini**

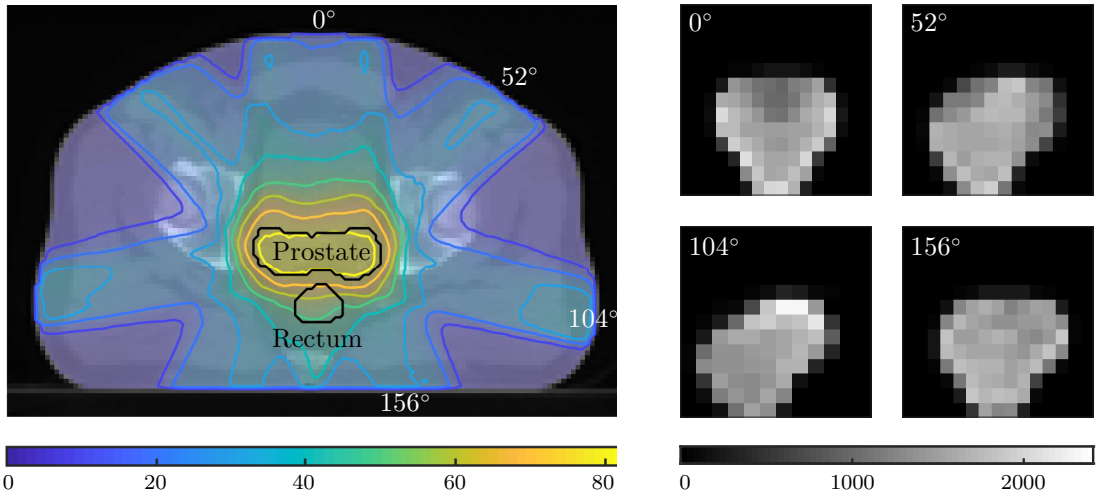


Figure 10 **Solution to Example 4.1. Left: The prostate tumor is irradiated by seven equally spaced beams with a dose-volume constraint on the rectum. Right: Beamlets intensities for four of the seven beams, calculated to deliver a nearly uniform dose of 81 Gy to the PTV while ensuring the no more than 50% of the OAR volume receives more than 50 Gy. Due to symmetry, the remaining three beams have similar intensity patterns.**

To further illustrate the tradeoff between the competing PTV and OAR objectives, we consider the same problem with increasingly more difficult dose-volume constraints on the rectum. In particular, we keep the target dose the same, but progressively decrease the dose d_2^{dv} and volume p of the dose-volume constraint. the dose-volume histograms for the dose-volume constraint that no more than 30% of the rectum receives more than 30 Gy

(Figure 11, top row). The model converges after 468 iterations, with 33.37% of the rectum volume receiving more than 30 Gy, as opposed to the initialization where 64.14% of the volume receives more than 30 Gy.

The dose-volume histograms for the dose-volume constraint that no more than 10% of the rectum volume receives more than 10 Gy (Figure 11, bottom row). In this case, the model converges after 320 iterations, with 23.91% of the rectum volume receiving more than 10 Gy, in contrast with the initialization where 73.97% of the volume receives more than 10 Gy. In general, as the constraint becomes more difficult, the dose to the rectum decreases while the dose to the tumor deviates more from the target uniform dose. If the dose-volume constraint makes the problem completely infeasible, the approach still returns some solution, but it need not meet the dose-volume constraint nor the target tumor dose.

4.2. One PTV and one OAR with multiple dose-volume constraints

Next we consider the problem of delivering a uniform dose of 81 Gy to the prostate tumor, with multiple dose-volume constraints on the rectum:

- No more than 0% of the rectum volume receives more than 75 Gy,
- no more than 20% of the rectum volume receives more than 60 Gy,
- no more than 50% of the rectum volume receives more than 50 Gy, and
- no more than 60% of the rectum volume receives more than 20 Gy.

The first dose-volume constraint corresponds to a maximum dose constraint, but expressing it as a dose-volume constraint allows us to apply our relaxation rather than enforce a hard constraint. As in the previous example, we use the linear beamlet-to-voxel map $A_1 \in \mathbb{R}^{6770\times 986}$ and dose vector $d_1 = 71 \cdot \mathbf{1} \in \mathbb{R}^{6770}$ for the PTV, along with the decision variable $x \in \mathbb{R}^{986}$ corresponding to the nonnegative beamlet intensities. However, for the OAR we need to introduce matrices $A_{21} = A_{22} = A_{23} = A_{24} = A_2 \in \mathbb{R}^{1764\times 986}$ and dose vectors $d_{21}^{\text{dv}} = 75 \cdot \mathbf{1} \in \mathbb{R}^{1764}$, $d_{22}^{\text{dv}} = 60 \cdot \mathbf{1} \in \mathbb{R}^{1764}$, $d_{23}^{\text{dv}} = 50 \cdot \mathbf{1} \in \mathbb{R}^{1764}$, and $d_{24}^{\text{dv}} = 20 \cdot \mathbf{1} \in \mathbb{R}^{1764}$, along with vectors $w_1, w_2, w_3, w_4 \in \mathbb{R}^{1764}$ corresponding to the deviation between the dose received by the rectum and the dose-volume constraints.

Using Algorithm 2, we converge after 568 iterations. In Figure 12, we see that some of the constraints have been met, while others are only approximately met. Specifically, 3.88% of the voxels exceed 75 Gy (initially 13.41%), 21.72% of the voxels exceed 60 Gy (initially 38.47%), 46.60% of the voxels exceed 50 Gy (initially 56.80%), and 61.41% of the

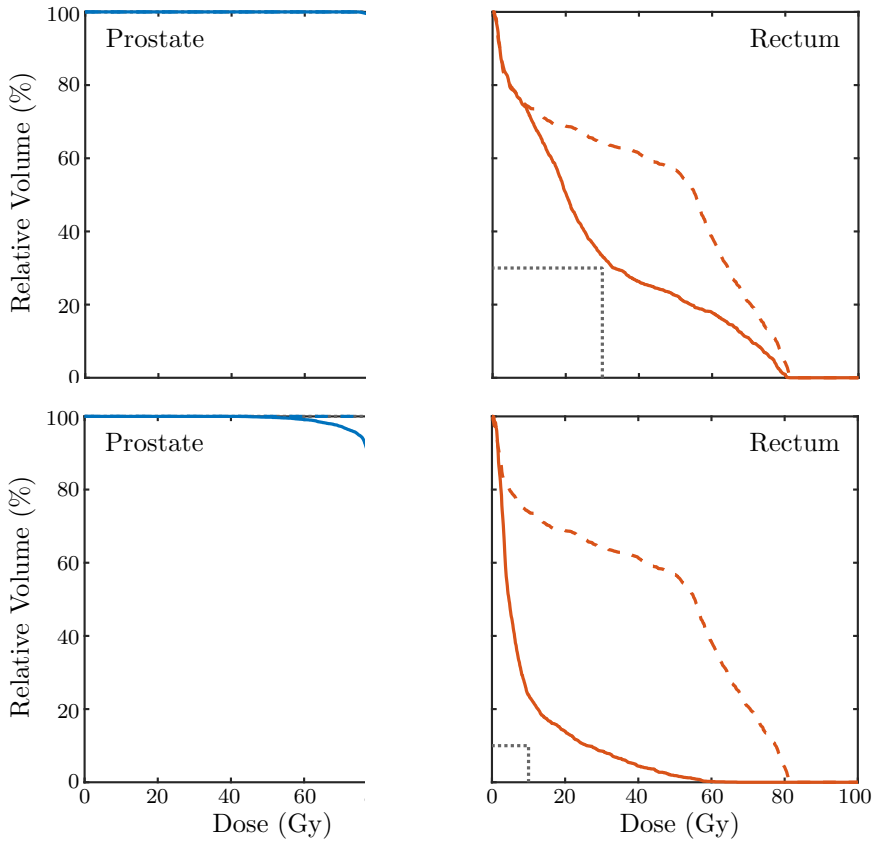


Figure 11 **Cumulative dose-volume histograms for Example 4.1 with progressively more difficult dose-volume constraints. Uniform target and dose-volume constraint are denoted by dotted lines, the initial dose by dashed lines, and the final dose by solid lines. As we reduce the dose and volume of the constraint to the OAR, the coverage of the PTV dose decreases. Top left: There is no notable difference between the initial and final dose to the PTV. Top right: The constraint that no more than 30% of the OAR volume receives more than 30 Gy is approximately met, with 33.37% of the volume exceeds 30 Gy, as opposed to the initialization where 64.14% does. Bottom left: The final dose to the PTV is noticeably worse than the initialization, with more of the volume deviating from the prescribed 81 Gy. Bottom right: The constraint that no more than 10% of the OAR volume receives more than 10 Gy is not met, with 23.91% of the volume exceeds 10 Gy, but this is drastic improvement on the initialization, where 73.97% of the volume exceeds 10 Gy.**

voxels exceed 20 Gy (initially 68.81%). Importantly, it is possible to specify the shape of the OAR dose-profile without any significant change to the PTV dose profile.

One downside to adding multiple dose-volume constraints on a particular OAR is the inclusion of more terms to the objective function, increasing the problem dimension. However, we can reduce the number of objective terms for the OAR, combining each individual dose-volume constraint term corresponding to organ j

$$\frac{\alpha_{jk}}{2n_j}\|w_{jk} - (A_j x - d_{jk}^{\mathrm{dv}})\|_2^2 \quad \text{s.t.} \quad \|(w_{jk})_+\|_0 \leq \frac{n_j p_{jk}}{100}$$

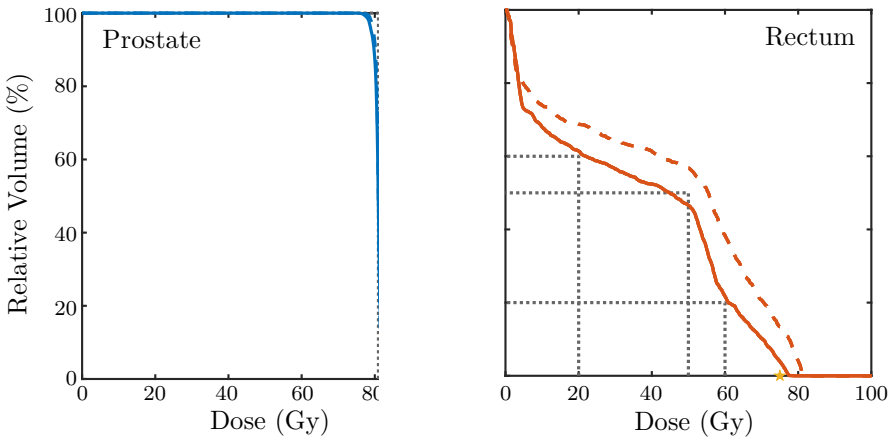


Figure 12 **Cumulative dose-volume histogram for Example 4.2. Uniform target and dose-volume constraint are denoted by dotted lines, the initial dose by dashed lines, and the final dose by solid lines. Left: There is no notable difference between the initial and final dose to the PTV. Right: The dose-volume constraints on the OAR are approximately met, with 3.88% of the volume exceeding 75 Gy (initial 13.14%, target 0%), 21.72% of the volume exceeding 60 Gy (initial 38.47%, target 20%), 46.60% of the voxels exceeding 50 Gy (56.80% initial, 50% target), and 61.41% of the volume exceeding 20 Gy (68.81% initial, 60% target).**

into one term

$$\frac{\alpha_j}{2n_j}\|y_j - A_j x\|_2^2 \quad \text{s.t.} \quad y_j \in \tilde{\Omega}_j,$$

where $\tilde{\Omega}_j = \Omega_{j1} \cap \cdots \cap \Omega_{jK_j}$ represents a set that satisfies all of the organ's dose-volume constraints. As long as the set of dose-volume constraints follows the pattern that doses increase as volumes decrease, projection onto this set can be computed efficiently by ordering the elements of y_j, allowing the highest $p_{jk}\%$ of voxels to exceed d_{jk}^{dv} and setting all remaining voxels above d_{jk}^{dv} to d_{jk}^{dv}, starting with the first dose-volume constraint (highest dose, lowest volume) and ending with the last dose-volume constraint (lowest dose, highest volume).

4.3. Multiple PTVs and OARs

Finally, we consider the problem of delivering a uniform dose of 81 Gy to the prostate tumor and a uniform dose of 60 Gy to tumors in the lymph nodes, while satisfying the dose-volume constraints that no more than 50% of the rectum receives more than 50 Gy and no more than 30% of the bladder receives more than 30 Gy. In addition to tumor and rectum structures $A_1 \in \mathbb{R}^{6770\times 986}$, $d_1 = 81 \cdot \mathbf{1} \in \mathbb{R}^{6770}$, $A_2 \in \mathbb{R}^{1648\times 986}$, $d_2^{\text{dv}} = 50 \cdot \mathbf{1} \in \mathbb{R}^{1648}$, and $w_2 \in \mathbb{R}^{1648}$, we introduce lymph node and bladder structures $A_3 \in \mathbb{R}^{8329\times 986}$, $d_3 = 60 \cdot \mathbf{1} \in \mathbb{R}^{8329}$, $A_4 \in \mathbb{R}^{9857\times 986}$, $d_4^{\text{dv}} = 30 \cdot \mathbf{1} \in \mathbb{R}^{9857}$, and $w_4 \in \mathbb{R}^{9857}$. We converge after 336 iterations of Algorithm 2.

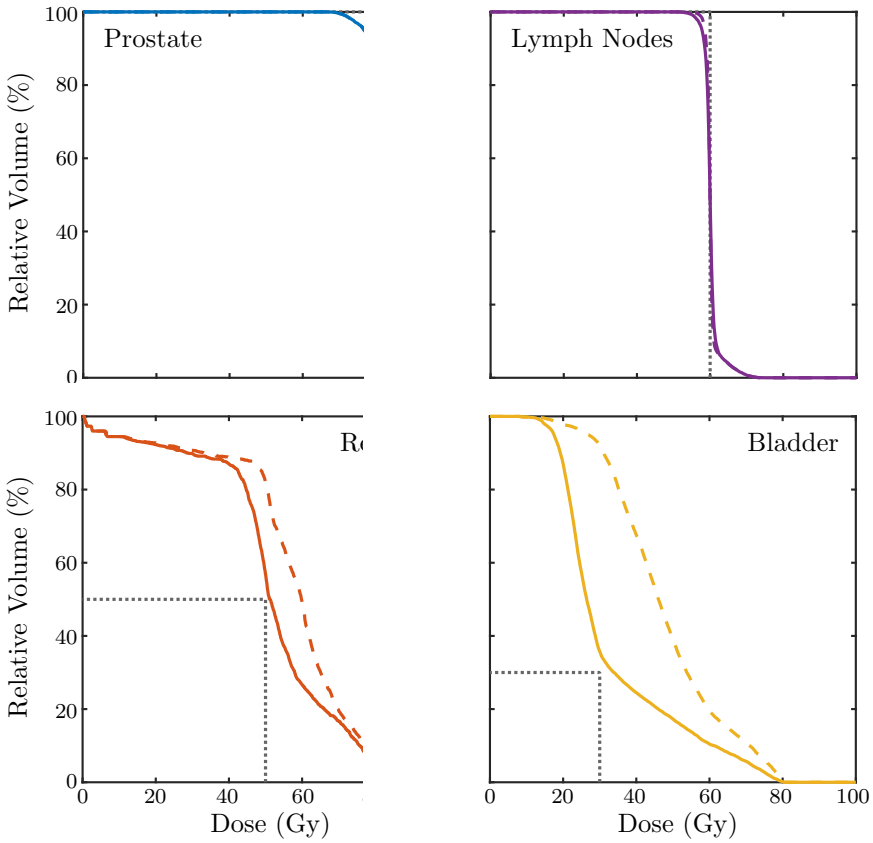


Figure 13 **Cumulative dose-volume histogram for Example 4.3. Uniform and dose-volume constraint targets are denoted by dotted lines, the initial dose by dashed lines, and the final dose by solid lines. Top row: There is little noticeable difference between the dose to the PTVs in the prostate and lymph nodes, though their proximity causes less prostate voxels to receive their target dose and more lymph node voxels to exceed their target dose than we would like. Bottom row: The dose-volume constraints to the OARs are approximately met, with 57.04% of the rectum exceeding 50 Gy (initial 81.04%, target 50%) and 35.76% of the bladder exceeding 30 Gy (initial 92.21%, target 30%).**

Due to the proximity of the two PTVs and the difference between their target doses, it is much more difficult to deliver a uniform dose to both targets. More of the prostate volume receives less than 81 Gy than in previous examples, while more of the lymph node volume exceeds 60 Gy than we would like (Figure 13, top row). In this case, it may be important to add lower and upper dose-volume constraints on the PTVs to ensure that appropriate doses are delivered. the dose-volume constraints on the rectum and bladder are both approximately met, with 57.04% of the rectum exceeding 50 Gy (initial 81.04%) and 35.76% of the bladder exceeding 30 Gy (initial 92.21%) (Figure 13, bottom row). The increase in competing objectives and geometric constraints results in more complicated beamlet intensity patterns and dose distributions, illustrated in Figure 14.

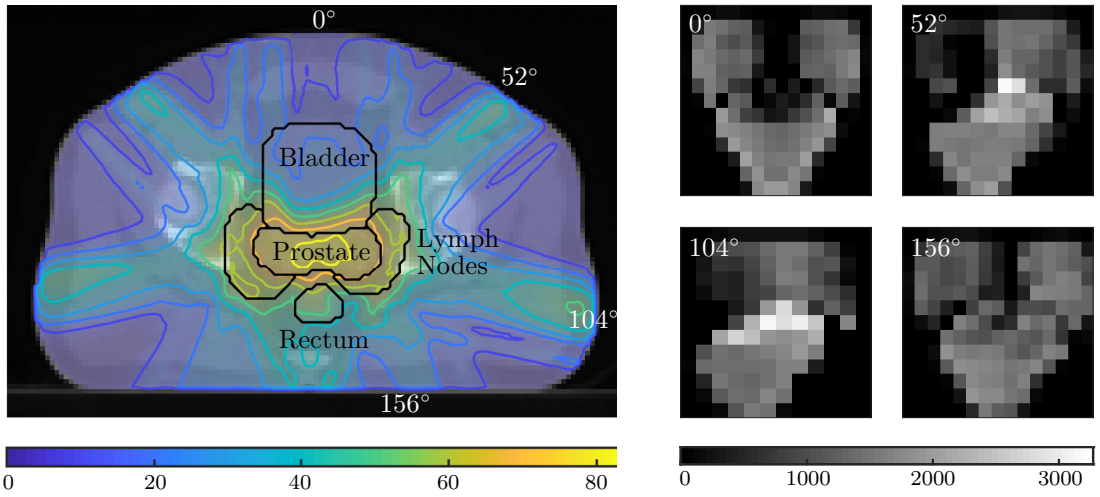


Figure 14 **Solution to Example 4.3. Right: Tumors in the prostate and lymph nodes are irradiated by seven equally spaced beams with dose-volume constraints on the rectum and bladder. Left: Beamlet intensities for four of the seven beams, calculated to deliver a nearly uniform dose of 81 Gy to the prostate and 60 Gy to the lymph nodes while ensuring that no more than 50% of the rectum volume receives more than 50 Gy and no more than 30% of the bladder volume receives more than 30 Gy. Due to symmetry, the remaining three beams have similar intensity patterns.**

5. Conclusions and future research

The main challenge of radiation treatment planning is to deliver a prescribed dose to the tumor while sparing surrounding healthy tissues. The fluence map optimization problem for intensity-modulated radiation therapy can be formulated as a large-scale inverse problem with competing objectives and constraints on the planning target volumes and organs-at-risk. Unfortunately, the clinically relevant dose-volume constraints are nonconvex, so solving treatment planning problems exactly with dose-volume constraints is NP-hard. We proposed a new approach that is well adapted to handle nonconvex dose-volume constraints without relying on convex relaxations. To solve this formulation, we developed a customized algorithm that is guaranteed to converge to a stationary point of the proposed model. The overall approach is scalable, handles multiple objectives on PTVs and OARs, and returns actionable treatment plans as demonstrated with examples on the CORT dataset.

While this paper focuses primarily on the methodology of our new approach, future work on this project will be directed towards practical considerations. We will test our model on additional datasets including different tumor types, patient geometries, and prescriptions. The comparison of the results using our approach and commercial treatment planning systems is left for future work.

References

[1] Radiation therapy to treat cancer, July 2017.

[2] Anders Brahme. Optimization of stationary and moving beam radiation therapy techniques. *Radiotherapy and Oncology*, 12(2):129–140, 1988.

[3] David M. Shepard, Michael C. Ferris, Gustavo H. Olivera, and T. Rockwell Mackie. Optimizing the delivery of radiation therapy to cancer patients. *SIAM Review*, 41(4):721–744, 1999.

[4] S. Webb. The physical basis of IMRT and inverse planning. *The British Journal of Radiology*, 76(910):678–689, 2003.

[5] Thomas Bortfeld. IMRT: a review and preview. *Physics in Medicine and Biology*, 51(13):R363–R379, 2006.

[6] Matthias Ehrgott, Çiğdem Güler, Horst W. Hamacher, and Lizhen Shao. Mathematical optimization in intensity modulated radiation therapy. *Annals of Operations Research*, 175(1):309–365, 2010.

[7] Spiridon V. Spirou and Chen-Shou Chui. A gradient inverse planning algorithm with dose-volume constraints. *Medical Physics*, 25(3):321–333, 1998.

[8] Mark Langer and Joseph Leong. Optimization of beam weights under dose-volume restrictions. *International Journal of Radiation Oncology Biology Physics*, 13(8):1255–1260, 1987.

[9] Philip E. Gill, Walter Murray, and Michael A. Saunders. SNOPT: An SQP algorithm for large-scale constrained optimization. *SIAM review*, 47(1):99–131, 2005.

[10] Steven M. Morrill, Richard G. Lane, Jorge A. Wong, and Isaac I. Rosen. Dose-volume considerations with linear programming optimization. *Medical Physics*, 18(6):1201–1210, 1991.

[11] Anqi Fu, Baris Ungun, Lei Xing, and Stephen Boyd. A convex optimization approach to radiation treatment planning with dose constraints. 2017.

[12] Jorge Llacer, Joseph O. Deasy, Thomas R. Bortfeld, Timothy D. Solberg, and Claus Promberger. Absence of multiple local minima effects in intensity modulated optimization with dose-volume constraints. *Physics in Medicine and Biology*, 48(2):183–210, 2003.

[13] Chuan Wu, Robert Jeraj, and Thomas R. Mackie. The method of intercepts in parameter space for the analysis of local minima caused by dose-volume constraints. *Physics in Medicine and Biology*, 48(11):N149–N157, 2003.

[14] J.O. Deasy. Multiple local minima in radiotherapy optimization problems with dose-volume constraints. *Medical Physics*, 24(7):1157–1161, 1997.

[15] R. Tyrrell Rockafellar. Lagrange multipliers and optimality. *SIAM review*, 35(2):183–238, 1993.

[16] Qiuwen Wu and Radhe Mohan. Multiple local minima in IMRT optimization based on dose-volume criteria. *Medical Physics*, 29(7):1514–1527, 2002.

[17] Thomas Bortfeld. Optimized planning using physical objectives and constraints. *Seminars in Radiation Oncology*, 9(1):20–34, 1999.

[18] Carl Graham Rowbottom and Steve Webb. Configuration space analysis of common cost functions in radiotherapy beam-weight optimization algorithms. *Physics in Medicine and Biology*, 47(1):65–77, 2002.

[19] Peng Zheng and Aleksandr Aravkin. Relax-and-split method for nonsmooth nonconvex problems. *arXiv preprint arXiv:1802.02654*, 2018.

[20] Aleksandr Aravkin and Damek Davis. Trimmed statistical estimation via variance reduction. *To appear in the Mathematics of Operations Research*, 2018.

[21] David Craft, Mark Bangert, Troy Long, Dávid Papp, and Jan Unkelbach. Shared data for intensity modulated radiation therapy (IMRT) optimization research: the CORT dataset. *GigaScience*, 3(1):37, 2014.